npj | Quantum Information

www.nature.com/npjqi

ARTICLE OPEN

Check for updates

Experimental realization of phase-controlled dynamics with hybrid digital–analog approach

Ziyu Tao[1,2,3,4,5], Libo Zhang[1,2,3,4,5], Xiaole Li[1,2,3,4], Jingjing Niu[1,2,3,4], Kai Luo[1,2,3,4], Kangyuan Yi[1,2,3,4], Yuxuan Zhou[1,2,3,4], Hao Jia[1,2,3,4], Xu Zhang[1,2,3,4], Song Liu[1,2,3,4✉], Tongxing Yan[1,2,3,4✉], Yuanzhen Chen[1,2,3,4✉] and Dapeng Yu[1,2,3,4]

Quantum simulation can be implemented in pure digital or analog ways, each with their pros and cons. By taking advantage of the universality of a digital route and the efficiency of analog simulation, hybrid digital–analog approaches can enrich the possibilities for quantum simulation. We use a hybrid approach to experimentally perform a quantum simulation of phase-controlled dynamics resulting from a closed-contour interaction (CCI) within certain multi-level systems in superconducting quantum circuits. Due to symmetry constraints, such systems cannot host an inherent CCI. Nevertheless, by assembling analog modules corresponding to their natural evolutions and specially designed digital modules constructed from standard quantum logic gates, we can bypass such constraints and realize an effective CCI in these systems. Based on this realization, we demonstrate a variety of related and interesting phenomena, including phase-controlled chiral dynamics, separation of chiral enantiomers, and a mechanism to generate entangled states based on CCI.

npj Quantum Information (2021)7:73 ; https://doi.org/10.1038/s41534-021-00406-1

INTRODUCTION

Digital quantum simulation relies on decomposition of the evolution of a targeted Hamiltonian into a sequence of discrete quantum logic gates[1–3]. While in principle this can be done for an arbitrary quantum system[4], it often requires an intimidating number of gate operations with high precision. Analog approaches exploiting the continuous nature of quantum evolutions may often be more efficient[5–8], but usually must be designed on an *adhoc* basis. Hybrid digital–analog quantum simulation has thus been proposed to combine the universality of digital approaches with analog efficiency[9–12]. The flexibility in engineering and assembling digital and analog modules generates abundant possibilities for quantum simulation that are hardly available otherwise. For example, in a simulation of the quantum Rabi model[13], a deep-strong coupling that is inaccessible to pure analog or digital approaches could be realized via a hybrid method[14].

In this work, we show that by employing a hybrid method, one can perform quantum simulations that may not be straightforward to implement via a direct mapping of the targeted Hamiltonian to the involved physical platform. In particular, we demonstrate phase-controlled quantum dynamics and related phenomena via closed-contour interaction (CCI) in superconducting quantum circuits, which was originally forbidden by certain symmetry-imposed selection rules. The simplest realization of CCI involves a three-level system. Such systems with two of the three possible transitions being coherently driven have been widely researched for both fundamental interest and promising applications in areas such as quantum sensing[15,16] and quantum information processing[17]. By opening the third transition, the three levels form a loop with a CCI, which leads to various quantum phenomena, including phase-dependent coherent population trapping[18], phase-controlled dynamics[19], and coherence protection[20]. A closed-loop configuration can also be used in the detection and separation of enantiomers[21–23], i.e., chiral molecules with left (*L*) and right (*R*) handedness, which has long been a challenging problem in chemistry[24].

In practice, the implementation of CCI is often hindered by selection rules for transitions imposed by symmetry constraints in realistic systems. Common practice in overcoming this problem includes the simultaneous use of multiple drivings of different types (e.g., both electric and magnetic dipole transitions)[20] or high-order processes such as a two-photon transition[25,26]. Here, we first show that in a three-level system subject to such selection rules, one can engineer the system Hamiltonian by assembling two digital and one analog module to induce a CCI with only two coherent drivings of the same type. Phenomena related to CCI, such as phase-controlled chiral dynamics, are observed. By making such driving fields time-dependent, we are able to demonstrate a proposed scheme to separate chiral molecules with high fidelity[27], and we can extend our technique to more complex systems. Specifically, we propose and realize a scheme to generate entangled states using a CCI across two coupled superconducting qubits.

RESULTS

Realization of CCI

Consider a three-level system composed of three states $\{|g\rangle, |e\rangle, |f\rangle\}$. The system is coherently driven by two external fields of the same type, such as electric-dipole allowed transitions, that correspond to $|g\rangle \leftrightarrow |e\rangle$ and $|e\rangle \leftrightarrow |f\rangle$. The effective Hamiltonian of the system under rotating-wave approximation is given by (see Methods section)

$$H_0 = \frac{\hbar}{2}\begin{pmatrix} -\Delta_A & \Omega_A^* & 0 \\ \Omega_A & 0 & \Omega_B^* \\ 0 & \Omega_B & \Delta_B \end{pmatrix}, \quad (1)$$

[1]Shenzhen Institute for Quantum Science and Engineering, Southern University of Science and Technology, 518055, Shenzhen, China. [2]Department of Physics, Southern University of Science and Technology, 518055, Shenzhen, China. [3]Guangdong Provincial Key Laboratory of Quantum Science and Engineering, Southern University of Science and Technology, 518055, Shenzhen, China. [4]Shenzhen Key Laboratory of Quantum Science and Engineering, Southern University of Science and Technology, 518055, Shenzhen, China. [5]These authors contributed equally: Ziyu Tao, Libo Zhang. ✉email: lius3@sustech.edu.cn; yantx@sustech.edu.cn; chenyz@sustech.edu.cn

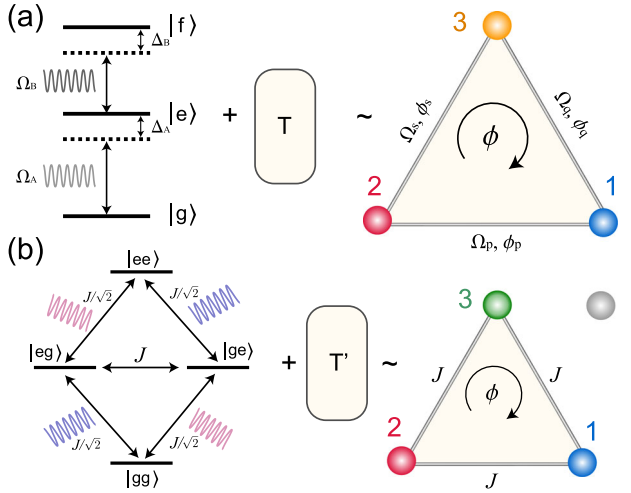

Fig. 1 Realization of CCI with a hybrid digital–analog approach. **a** A three-level system (a qutrit) driven by two detuned external fields (described by a Hamiltonian of H_0), when combined with specially designed digital modules (the T block) constructed from discrete quantum gates, can be used to realize the Hamiltonian H hosting an inherent CCI: $Te^{-iH_0t}T^\dagger \equiv e^{-iHt}$, with a gauge-invariant phase ϕ. For consistency with the literature, we relabel the states of the qutrit as $|g\rangle, |e\rangle, |f\rangle = 1, 2, 3$. **b** In a similar way, combining the natural evolution of two resonant qutrits driven by two external fields (with identical amplitudes and phases, indicated by different colors) with certain digital modules can result in a CCI in a subspace of the system. Here 1, 2, and 3 correspond to $|gg\rangle$, $|ge\rangle$, and $|eg\rangle$, respectively. The gray sphere beside the state of three represents a dark state that is decoupled from the evolution of the system (see Methods section).

where $\Omega_{A,B}$ and $\Delta_{A,B}$ are the amplitudes and detunings, respectively, of the two external driving fields (see Fig. 1a).

If the system assumes a restrictive symmetry, then the third transition $|g\rangle \leftrightarrow |f\rangle$ of the same type is forbidden. Even in systems of less restrictive symmetry (e.g., artificial atoms such as superconducting qubits), the amplitude of such transitions is usually vanishingly small[28]. Previously, a third driving of a different type or of the same type but of higher order was used to close the loop to form a CCI[25,26]. We take a different approach by combining an analog module corresponding to the evolution driven by H_0 with two digital modules that are unitary operators constructed from standard quantum gates (see the flowchart on top of Fig. 2a). Now the effective Hamiltonian resulted from the three combined modules can be obtained via $e^{-iHt/\hbar} \equiv Te^{-iH_0t/\hbar}T^\dagger$ (the matrix form of T and $T^\dagger$ is given in the Methods section). If the amplitudes and detunings of the two drivings in H_0 are set to $\Omega_A = \left[\Omega_p e^{i\phi_p} + \Omega_s e^{i(-\phi_q-\phi_s)}\right]/\sqrt{2}$, $\Omega_B = \left[-\Omega_p e^{i(-\phi_q-\phi_p)} + \Omega_s e^{i\phi_s}\right]/\sqrt{2}$, $\Delta_{A,B} = -\Omega_q$, one obtains:

$$H = \frac{\hbar}{2}\begin{pmatrix} 0 & \Omega_p e^{-i\phi_p} & \Omega_q e^{i\phi_q} \\ \Omega_p e^{i\phi_p} & 0 & \Omega_s e^{-i\phi_s} \\ \Omega_q e^{-i\phi_q} & \Omega_s e^{i\phi_s} & 0 \end{pmatrix}. \quad (2)$$

This Hamiltonian differs from H_0 in that it naturally contains nonzero amplitudes for all three possible transitions, and the magnitudes and phases of all three amplitudes can be adjusted independently (see Fig. 1a). Therefore, inherent CCI dynamics can be expected for such a Hamiltonian. In the case of equal and constant magnitudes, $\Omega_{p,q,s} \equiv \Omega$, the population dynamics are strongly dependent on the phases $\phi_{p,s,q}$ of the driving fields, through a gauge-invariant global phase $\phi = \phi_p + \phi_s - \phi_q$. We will show an experimental demonstration of such CCI dynamics.

We used Xmon-type superconducting qutrits in our experimental work. In this kind of artificial atom, the transitions of $|g\rangle \leftrightarrow |e\rangle$ and $|e\rangle \leftrightarrow |f\rangle$ are electric-dipole allowed, whereas the transition $|g\rangle \leftrightarrow |f\rangle$ of the same type has a vanishingly small amplitude[28]. Two external microwave driving fields in the forms described above ($\Omega_{A,B}$) are applied to the qutrit, with $\Omega_{p,q,s} \equiv \Omega$ and three independently adjustable phases $\phi_{p,q,s}$. Probability of states is measured and normalized following a procedure widely adapted by the community (see Methods section for details), and is used for subsequent data analysis. More details of the experimental setup can be found in the Supplementary Note 1.

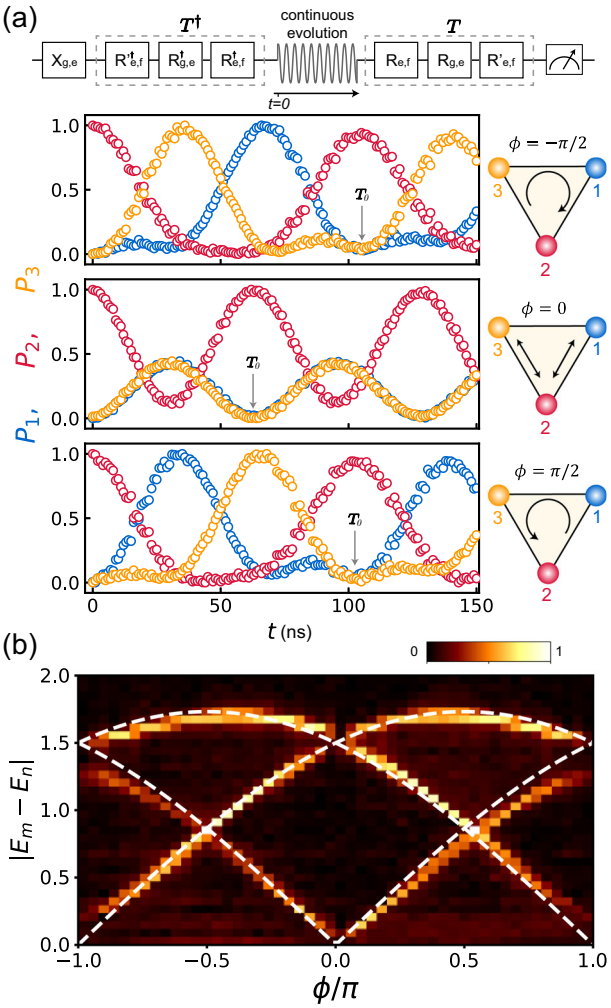

Fig. 2 Phase-controlled quantum dynamics resulting from CCI in a single qutrit. **a** Upper part: flowchart of the experiment, including a block for initialization ($X_{g,e}$), a digital module of $T^\dagger$ composed of three gate operations, an analog module of the natural evolution driven by H_0, and another digital module T, followed by projection measurements that yield the three populations of $P_{1,2,3}$. Both ramp-on and -off time of the continuous microwave driving in the analog module is <1 ns. The effect of such a finite ramping time is negligible since observing the CCI and analyzing the related physics require a time scale much longer. Lower part: $P_{1,2,3}$ as functions of the time span of the intermediate natural evolution for three values of the gauge-invariant parameter ϕ. **b** Energy spectrum of the Hamiltonian of H in Eq. (2), obtained via discrete Fourier transform of the measured populations. It is shown in the form of $|E_m - E_n|$, where E_k are the eigenenergies of H, and $m, n \in \{1, 2, 3\}$. Dashed white lines represent theoretical predictions.

CCI dynamics

We first study the CCI dynamics of the system by measuring its time evolution at different values of ϕ. Figure 2a shows the temporal sequence of operations. The system is initialized in the

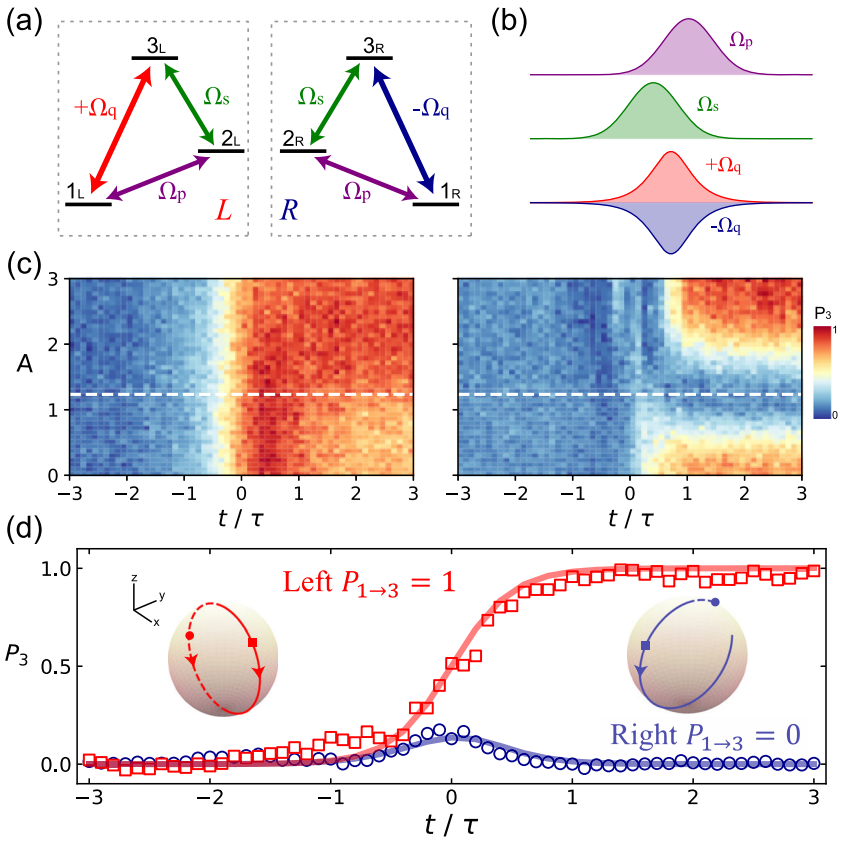

Fig. 3 Chiral separation via CCI. a Coupling schemes of chiral molecules with *L* and *R* handedness. Identical drivings result in a difference of π in the overall phase of the loop, indicated here as different couplings ($\pm\Omega_q$) between the states of 1 and 3. **b** Pulse sequence for the driving fields $\Omega_p(t)$, $\Omega_s(t)$, and $\pm\Omega_q(t)$. **c** Measured population P_3 versus time and pulse area $A\pi$ for *L* (left panel) and *R* (right panel) handedness, where the initial state $|\psi_0\rangle = |1\rangle$. The maximum population contrast is obtained when $A \approx 1.23$ (indicated by the white dashed lines). $t = 0$ corresponds to the moment when the $\pm\Omega_q$ pulse reaches its maximum magnitude. **d** The population P_3 as a function of time for $A = 1.23$, showing that the transfer to the state of three is nearly perfect for *L* handedness, but completely suppressed for *R* handedness. The spheres illustrate the trajectories of state evolution in the Majorana representation by mapping the qutrit states to two points on the spheres[42] (see Supplementary Note 4).

first excited state of $|\psi(t=0)\rangle = |e\rangle$ by a standard *X* gate. A digital module containing three quantum gates is applied to the qutrit, followed by an analog evolution driven by H_0 with two control parameters: the time span and the gauge-invariant phase ϕ. Another digital module, which is the Hermitian conjugate of the first digital module, is applied, followed by projection measurements that yield populations of all three states. As discussed previously, the combined effect of the middle three blocks is to subject the system to evolve under the Hamiltonian *H* as in Eq. (2): $e^{-iHt/\hbar} \equiv Te^{-iH_0t/\hbar}T^\dagger$ (see Methods section for details).

The gauge-invariant phase ϕ assumes a role as the flux of a synthetic magnetic field, which controls the dynamics of the system. At $\phi = 0$, the populations evolve in time with a symmetric pattern without a preferred direction of circulation (middle panel, Fig. 2a). Such symmetry in the circulation pattern is not observed for values of ϕ that are not integers of π. Two examples corresponding to $\phi = \pm\pi/2$ are shown in Fig. 2a. In each case, a circulation of certain chirality is observed: clockwise for $\phi = -\pi/2$ and counterclockwise for $\phi = \pi/2$. Such differences are rooted in the symmetry of the system upon time reversal. An examination of the time-reversal symmetry (TRS) in a strict sense requires reversing the flow of time, which is of course not experimentally feasible. However, the periodicity presented in the evolutions shown in Fig. 2a allows for a practical definition of the TRS: $\psi(t) = \psi(T_0 - t)$, where T_0 is the period of a given evolution[5]. By comparing the evolutions from $t = 0$ forward and from $t = T_0$ backward, Fig. 2a shows that the TRS is preserved for $\phi = 0$, but broken for $\phi = \pm\pi/2$.

In addition to demonstrating the phase-controlled dynamics under CCI, we mapped out the electronic structure of the system as a function of ϕ. The eigenenergies of *H* are given by $E_k = \Omega\cos[\phi/3 - \varphi_0(k+1)]$, with $k \in \{1, 2, 3\}$ and $\varphi_0 = 2\pi/3$. A Fourier transformation of the measured populations can reveal the energy differences $|E_m - E_n|$ with $m, n \in \{1, 2, 3\}$ and $m \neq n$, as shown in Fig. 2b, which agree with the simulated results using *H* in Eq. (2). The anti-crossings at $\phi = \pm\pi$ in the spectrum can be explained by the slight detuning of the coherent drives and environmental fluctuations[20].

Chiral separation

Beyond constant driving fields, we further consider a closed loop driven by three time-dependent fields $\Omega_p(t)$, $\Omega_s(t)$, and $\Omega_q(t)$, which was proposed to detect and separate enantiomers with *L* and *R* handedness by using the phase-sensitive interferometric nature of the closed-loop configuration[27].

For a three-level system subjected to a pumping drive $\Omega_p(t)$ ($|1\rangle \leftrightarrow |2\rangle$) and Stokes drive $\Omega_s(t)$ ($|2\rangle \leftrightarrow |3\rangle$) (see Fig. 3a; for consistency with the literature, here we label the three states as $|1\rangle$, $|2\rangle$, and $|3\rangle$), the three eigenenergies and corresponding eigenstates are $\lambda_\pm = \pm\sqrt{\Omega_p^2 + \Omega_s^2}$, $\lambda_0 = 0$, and $|\chi_\pm\rangle = (\sin\theta|0\rangle \pm |2\rangle + \cos\theta|3\rangle)$, $|\chi_0\rangle = \cos\theta|1\rangle - \sin\theta|3\rangle$, with $\tan\theta(t) = \Omega_p(t)/\Omega_s(t)$. In the celebrated technique of stimulated

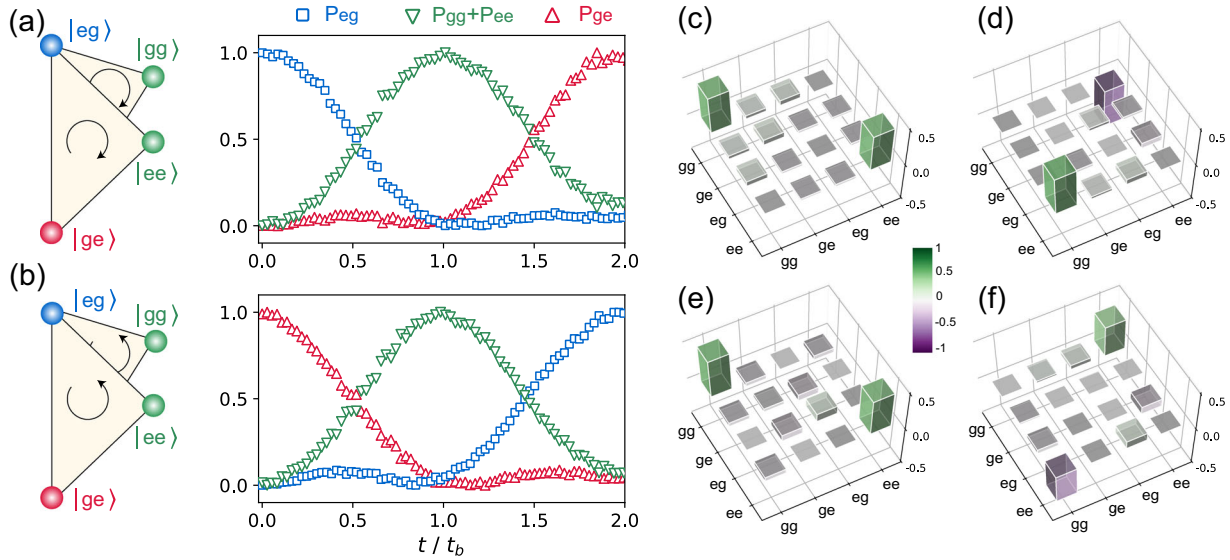

Fig. 4 Generation of entangled states using CCI. a, **b** The measured populations of P_{eg}, P_{ge}, and $P_{gg}+P_{ee}$. The non-entangled states $|eg\rangle$ and $|ge\rangle$ in **a** and **b** evolve into the entangled states of $(|gg\rangle \pm i|ee\rangle)/\sqrt{2}$ within time t_b under the maximum TRS breaking condition $\phi = \pm\pi/2$. **c** Real and **d** imaginary parts of the density matrix for the entangled state of $(|gg\rangle + i|ee\rangle)/\sqrt{2}$, constructed from data obtained by quantum state tomography. **e** Real and **f** imaginary parts for the state of $(|gg\rangle - i|ee\rangle)/\sqrt{2}$.

Raman adiabatic passage[29,30], the two pulses are arranged in a counterintuitive order with the Stokes pulse coming first, and the eigenstate $|\chi_0\rangle$ evolves adiabatically from $|1\rangle$ to $-|3\rangle$ as θ varies from 0 to $\pi/2$, thus accomplishing a nearly perfect state transfer coherently.

It has been shown that by adding a counterdiabatic driving $\Omega_q(t)$ ($|1\rangle \leftrightarrow |3\rangle$) to close the loop, the resultant dynamics of the population become dependent on the handedness of the system[31,32]. In particular, with the same driving fields, the Hamiltonian of the system is $H^{L,R} = (\Omega_p|2\rangle\langle 1| + \Omega_s|3\rangle\langle 2| \pm \Omega_q e^{i\phi}|3\rangle\langle 1|) + H.c.$ (Fig. 3a), where the $+(-)$ sign is for $L(R)$ handedness, and $H.c$ is the Hermitian conjugate. Such a sign difference will result in the same counterdiabatic driving doubling or canceling the nonadiabatic coupling presented in the system, depending on its handedness. If ϕ is set to $-\pi/2$, then the populations of the final state, P_3, of the enantiomers with L and R handedness are different. For example, with carefully chosen values of the pulse areas, the handedness can be efficiently determined by measuring P_3 alone, where $P_3 = 1 (P_3 = 0)$ for $L(R)$ handedness[27]. We note that such a counterdiabatic driving was originally proposed to accelerate various adiabatic processes, but here its major effect is to differentiate the L and R handedness.

We use pump and Stokes pulses of a Gaussian form in our experiment: $\Omega_p(t) = \Omega_0 e^{-(t-\tau/2)^2/\tau^2}$, $\Omega_s(t) = \Omega_0 e^{-(t+\tau/2)^2/\tau^2}$. Both pulses have a width of τ and are delayed by the same amount. A third pulse in the form of $\Omega_q(t) = \pm 2\dot{\theta}(t)$ is applied, where the $+(-)$ sign corresponds to $L(R)$ handedness. We prepare the system in an initial state of $|\chi_0\rangle$. As discussed above, for L handedness, the nonadiabatic transition is canceled by $\Omega_q(t)$ and the system remains in the state $|\chi_0\rangle$, inducing a perfect population transfer from $|1\rangle$ to $|3\rangle$ with $P_{1\to 3} = 1$ as $\theta(t)$ evolves from 0 to $\pi/2$. Conversely, for R handedness, the nonadiabatic transition doubles, which enables $|\chi_0\rangle \to |\chi_\pm\rangle$ and $P_{1\to 3} < 1$. Figure 3c shows the time evolution of P_3 with different pulse areas $A\pi$, which is defined as $\int \Omega_{p,s} dt = \Omega_0 \tau\sqrt{\pi} \equiv A\pi$. At $A \approx 1.23$, the driving fields $\Omega_{p,s,q}$ in the form of Fig. 3b result in a maximum distinguishability between a population transfer $|1\rangle \to |3\rangle$ for L handedness with $P_{1\to 3} = 0.986$ and the same transfer for R handedness with $P_{1\to 3} = 0.003$ (Fig. 3d). This result is expected following the original theoretical proposal[27].

Entanglement generation with CCI

Next, we extend the generation of CCI via pure microwave drivings to a more complex system of two coupled qubits, and further demonstrate a mechanism of entangling two qubits based on CCI, different from existing schemes that are widely used in quantum information processing with superconducting quantum circuits.

Consider the four-level system formed by two Xmon superconducting qubits with a coupling strength of J (see Fig. 1b). We apply two transverse resonant driving fields to the two qubits, with an identical amplitude of $J/\sqrt{2}$ and a phase difference of $\phi_a - \phi_b = \phi$. Similar to the single-qubit case discussed above, we combine the natural evolution of such a driven system (an analog module) and a unitary operation T' (two digital modules implemented via standard gate operations) to realize an effective Hamiltonian for a three-state system $\{|eg\rangle, |ge\rangle, |gg\rangle\}$ that can host CCI (see Fig. 1b and Methods section). Furthermore, we can generate entangled states of the two qubits by removing the unitary operation T', since it transforms the entangled state $|gg\rangle + e^{i\phi}|ee\rangle$ to the ground state $|gg\rangle$.

Specifically, the two-qubit system can be directly transferred from the non-entangled state $|eg\rangle$ or $|ge|$ to the maximum entangled states of $(|gg\rangle \pm i|ee\rangle)/\sqrt{2}$ (Fig. 4a, b), within a time of $t_b = 2\pi/(3\sqrt{3}J)$, under the condition of maximum TRS breaking at $\phi = \pm\pi/2$. The density matrices $\rho_\pm$ of the entangled states $|\psi_\pm\rangle$ characterized by quantum state tomography are given in Fig. 4c–f, with fidelities of $F_+ = 0.963 \pm 0.026$ and $F_- = 0.923 \pm 0.029$. The analytical form of the nontrivial two-qubit unitary operator e^{-iHt_b} is given in the Supplementary Note 3.

This mechanism of generating entanglement based on chiral CCI dynamics is different from the previous constructions of iSWAP[33,34] and controlled-Z gates[35–37], formed by the subspace $\{|ge\rangle, |eg\rangle\}$ or $\{|ee\rangle, |fg\rangle\}$ in superconducting qubits. Using a geometric classification of two-qubit gates developed by Zhang et al.[38], we have found that the specific implementation of this mechanism as reported here results in a class of perfect entangler that can generate maximally entangled two-qubit states. We have

also verified that this class is locally inequivalent to other commonly known methods (e.g., CNOT, iSWAP, iPhase, $\sqrt{\text{iSWAP}}$) for generating entanglement between two qubits in the sense that they cannot be linked via local operations acting on single qubits. Moreover, the technique used here utilizes two continuous microwave drivings that are independently adjustable. Such extra flexibility makes it possible to use the current technique, with proper adjustments of parameter settings, to realize other classes of two-qubit entangler, such as a B gate that is known to be one of the most efficient entanglers[39].

DISCUSSION

We have proposed and experimentally demonstrated an effective realization of CCI in genuine three-level systems that do not host CCI inherently due to certain symmetry constraints. By assembling an analog module of the natural evolution governed by their original Hamiltonians with carefully designed digital modules, we can effectively bypass such constraints and establish a CCI without auxiliary driving signals that are technically challenging to implement. Based on such a CCI, we can demonstrate a variety of interesting related phenomena such as a phase-controlled chiral dynamics, chiral separation, and a mechanism to generate entangled states.

The hybrid digital–analog approach used here is essential to our work, since on the one hand the above symmetry constraints forbid an inherent CCI that would manifest in the analog evolutions of the systems, and on the other hand, a pure digital approach is practically infeasible, as too many quantum gate operations would be required, especially to simulate the natural evolutions of the systems. This work serves as a preliminary demonstration of the enriched possibilities for quantum simulation by the hybrid digital–analog approach. One can reasonably expect, by assembling more sophisticated and ingeniously engineered analog and digital modules, the realm of quantum simulation that is accessible by pure analog or digital approaches can be largely expanded, a welcome development before we realize a universal and fault-tolerant digital quantum computer.

METHODS

Experimental setup

We used the Xmon-type of superconducting qutrit with a tunable frequency via a bias current on a Z-control line. Microwave pulses are applied to the qutrit via an XY-control line. All quantum gates in the digital modules have a time span of 20 ns. The state of the qutrit can be deduced by measuring the transmission coefficient S_{21} of the transmission line using a standard dispersive measurement[40]. For each data set in the main text, the displayed probability of states is obtained by processing the raw data using the following procedure of normalization. Prior to each measurement, the qutrit is successively prepared into the g, e, f states, and in each case p_g, p_e, p_f are measured. All nine acquired probabilities are then arranged into a readout matrix $\mathcal{R}$, which is used for normalizing all subsequent measurements. For example, a raw data set of $\overrightarrow{p} = (p_g, p_e, p_f)^T$ is multiplied with the inverse of $\mathcal{R}$ to obtain the normalized probability of states $\mathcal{R}^{-1} \cdot \overrightarrow{p}$. For the part of experiment involving two qubits, they are coupled via an ancillary qubit that can fine tune the effective coupling strength[41]. Further details of the samples and measurement setup can be found in the Supplementary Note 1.

Effective Hamiltonian of the three-level system

The effective Hamiltonian of the microwave-driven qutrit in a rotating frame is described by Eq. (1) in the main text. Here going into the rotating frame is realized via a transform of $U = |g\rangle\langle g| + |e\rangle\langle e|e^{i\omega_A t} + |f\rangle\langle f|e^{i(\omega_A t+\omega_B t)}$, where $\omega_A \equiv \omega_{ge} - \Delta_A$, $\omega_B \equiv \omega_{ef} - \Delta_B$ (see Fig. 1 for definitions of terms). Under the rotating-wave approximation, H_0 in Eq. (1) is resulted. The unitary operator T that serves as a digital module is

$$T = \begin{pmatrix} 1/\sqrt{2} & 0 & -e^{i\phi_q}/\sqrt{2} \\ 0 & 1 & 0 \\ e^{-i\phi_q}/\sqrt{2} & 0 & 1/\sqrt{2} \end{pmatrix}, \tag{3}$$

which can be constructed from three single-qutrit gates $R_{e,f}(\pi, 0) \cdot R_{g,e}(\pi/2, -\phi_q) \cdot R_{e,f}(\pi, \pi)$, where $R_{m,n}(\theta, \phi)$ represents a rotation in the subspace of $\{|m\rangle, |n\rangle\}$:

$$R_{m,n}(\theta, \phi) = \begin{pmatrix} \cos(\theta/2) & -e^{-i\phi}\sin(\theta/2) \\ e^{i\phi}\sin(\theta/2) & \cos(\theta/2) \end{pmatrix}. \tag{4}$$

The combination of the natural evolution of the original Hamiltonian and the unitary operations gives the effective Hamiltonian H in Eq. (2): $e^{-iHt/\hbar} \equiv Te^{-iH_0 t/\hbar}T^\dagger$, which describes a three-level system with CCI.

Effective Hamiltonian of the four-level system

Consider the four-level system formed by two coupled superconducting qubits with a coupling strength of J. We apply two transverse resonant driving fields, one to each qubit, with identical frequency $\omega_a = \omega_b = \omega_{ge}$ and amplitude $|\Omega_A| = |\Omega_B| = J/\sqrt{2}$, and a phase difference of $\phi_a - \phi_b = \phi$. In a rotating frame realized via a transform of $U = (|g\rangle\langle g| + |e\rangle\langle e|e^{i\omega_a t}) \otimes (|g\rangle\langle g| + |e\rangle\langle e|e^{i\omega_b t})$ and under the rotating-wave approximation, the Hamiltonian is given by

$$\begin{aligned} H/\hbar &= J(\cos\phi\sigma_x^a + \sin\phi\sigma_y^a + \sigma_x^b)/\sqrt{2} + J(\sigma_x^a \otimes \sigma_x^b + \sigma_y^a \otimes \sigma_y^b)/2 \\ &= \frac{J}{\sqrt{2}} \begin{pmatrix} 0 & 1 & e^{-i\phi} & 0 \\ 1 & 0 & \sqrt{2} & e^{-i\phi} \\ e^{i\phi} & \sqrt{2} & 0 & 1 \\ 0 & e^{i\phi} & 1 & 0 \end{pmatrix}. \end{aligned} \tag{5}$$

Combining the natural evolution governed by this Hamiltonian and a unitary operation defined as

$$T' = \frac{1}{\sqrt{2}} \begin{pmatrix} 1 & 0 & 0 & e^{-i\phi} \\ 0 & \sqrt{2} & 0 & 0 \\ 0 & 0 & \sqrt{2} & 0 \\ -e^{i\phi} & 0 & 0 & 1 \end{pmatrix} \tag{6}$$

gives an effective Hamiltonian H' via $e^{-iH't/\hbar} \equiv T'e^{-iHt/\hbar}T'^\dagger$:

$$H' = J\left(|eg\rangle\langle ge| + |ge\rangle\langle gg| + e^{i\phi}|eg\rangle\langle gg| + H.c.\right). \tag{7}$$

This Hamiltonian describes a three-level system with CCI. If the two unitary operations, T' and $T'^\dagger$ are dropped, then Eq. (7) becomes

$$\overline{H'} = J\left(|1\rangle\langle 2| + |2\rangle\langle 3| + e^{i\phi}|1\rangle\langle 3| + H.c.\right). \tag{8}$$

Here, $\{|1\rangle, |2\rangle, |3\rangle\}$ form an invariant triplet subspace of the overall Hilbert space of $\{|1\rangle, |2\rangle, |3\rangle, |D\rangle\} \equiv \{|eg\rangle, |ge\rangle, (|gg\rangle + e^{i\phi}|ee\rangle)/\sqrt{2}, (|gg\rangle - e^{i\phi}|ee\rangle)/\sqrt{2}\}$, and the state of $|D\rangle$ is a dark state that is decoupled from the system evolution.

DATA AVAILABILITY

The data supporting the findings of this study are available by the corresponding author upon request.

CODE AVAILABILITY

All codes used in the paper are available from the corresponding authors upon reasonable request.

Received: 13 November 2020; Accepted: 19 March 2021;
Published online: 18 May 2021

REFERENCES

1. Georgescu, I. M., Ashhab, S. & Nori, F. Quantum simulation. *Rev. Mod. Phys.* **86**, 153–185 (2014).
2. Barends, R. et al. Digital quantum simulation of fermionic models with a superconducting circuit. *Nat. Commun.* **6**, 7654 (2015).

3. Barends, R. et al. Digitized adiabatic quantum computing with a superconducting circuit. *Nature* **534**, 222–226 (2016).
4. Lloyd, S. Universal quantum simulators. *Science* **273**, 1073–1078 (1996).
5. Roushan, P. et al. Chiral ground-state currents of interacting photons in a synthetic magnetic field. *Nat. Phys.* **13**, 146–151 (2016).
6. Wang, D. W. et al. Synthesis of antisymmetric spin exchange interaction and chiral spin clusters in superconducting circuits. *Nat. Phys.* **15**, 382–386 (2019).
7. Cai, W. et al. Observation of topological magnon insulator states in a superconducting circuit. *Phys. Rev. Lett.* **123**, 080501 (2019).
8. Liu, W., Feng, W., Ren, W., Wang, D.-W. & Wang, H. Synthesizing three-body interaction of spin chirality with superconducting qubits. *Appl. Phys. Lett.* **116**, 114001 (2020).
9. Mezzacapo, A. et al. Digital quantum rabi and dicke models in superconducting circuits. *Sci. Rep.* **4**, 7482 (2015).
10. Lamata, L. Digital-analog quantum simulation of generalized dicke models with superconducting circuits. *Sci. Rep.* **7**, 43768 (2017).
11. Lamata, L., Parra-Rodriguez, A., Sanz, M. & Solano, E. Digital-analog quantum simulations with superconducting circuits. *Adv. Phys. X* **3**, 1457981 (2018).
12. Parra-Rodriguez, A., Lougovski, P., Lamata, L., Solano, E. & Sanz, M. Digital-analog quantum computation. *Phys. Rev. A* **101**, 022305 (2020).
13. Rabi, I. I. On the process of space quantization. *Phys. Rev.* **49**, 324–328 (1936).
14. Langford, N. K. et al. Experimentally simulating the dynamics of quantum light and matter at deep-strong coupling. *Nat. Commun.* **8**, 1715 (2017).
15. Phillips, D. F., Fleischhauer, A., Mair, A., Walsworth, R. L. & Lukin, M. D. Storage of light in atomic vapor. *Phys. Rev. Lett.* **86**, 783–786 (2001).
16. Vanier, J. Atomic clocks based on coherent population trapping: a review. *Appl. Phys. B* **81**, 421–442 (2005).
17. Cirac, J. I., Zoller, P., Kimble, H. J. & Mabuchi, H. Quantum state transfer and entanglement distribution among distant nodes in a quantum network. *Phys. Rev. Lett.* **78**, 3221–3224 (1997).
18. Kosachiov, D. V., Matisov, B. G. & Rozhdestvensky, Y. V. Coherent phenomena in multilevel systems with closed interaction contour. *J. Phys. B At. Mol. Opt. Phys.* **25**, 2473–2488 (1992).
19. Buckle, S. J. et al. Atomic interferometers: phase-dependence in multilevel atomic transitions. *Opt. Acta* **33**, 1129–1140 (1986).
20. Barfuss, A. et al. Phase-controlled coherent dynamics of a single spin under closed-contour interaction. *Nat. Phys.* **14**, 1087–1091 (2018).
21. Král, P. & Shapiro, M. Cyclic population transfer in quantum systems with broken symmetry. *Phys. Rev. Lett.* **87**, 183002 (2001).
22. Král, P., Thanopulos, I., Shapiro, M. & Cohen, D. Two-step enantio-selective optical switch. *Phys. Rev. Lett.* **90**, 033001 (2003).
23. Ye, C., Zhang, Q. & Li, Y. Real single-loop cyclic three-level configuration of chiral molecules. *Phys. Rev. A* **98**, 063401 (2018).
24. Knowles, W. S. Asymmetric hydrogenations. *Angew. Chem. Int. Ed. Engl.* **41**, 1998 (2002).
25. Vepsäläinen, A., Danilin, S. & Sorin Paraoanu, G. Superadiabatic population transfer in a three-level superconducting circuit. *Sci. Adv.* **5**, 5999 (2019).
26. Vepsäläinen, A. & Paraoanu, G. S. Simulating spin chains using a superconducting circuit: gauge invariance, superadiabatic transport, and broken time-reversal symmetry. *Adv. Quant. Technol.* **2020**, 1900121 (2020).
27. Vitanov, N. V. & Drewsen, M. Highly efficient detection and separation of chiral molecules through shortcuts to adiabaticity. *Phys. Rev. Lett.* **122**, 173202 (2019).
28. Koch, J. et al. Charge-insensitive qubit design derived from the Cooper pair box. *Phys. Rev. A* **76**, 1–19 (2007).
29. Vitanov, N. V., Rangelov, A. A., Shore, B. W. & Bergmann, K. Stimulated raman adiabatic passage in physics, chemistry, and beyond. *Rev. Mod. Phys.* **89**, 015006 (2017).
30. Bergmann, K. et al. Roadmap on STIRAP applications. *J. Phys. B At. Mol. Opt. Phys.* **52**, 202001 (2019).
31. Chen, X., Lizuain, I., Ruschhaupt, A., Guéry-Odelin, D. & Muga, J. G. Shortcut to adiabatic passage in two- and three-level atoms. *Phys. Rev. Lett.* **105**, 123003 (2010).
32. Guéry-Odelin, D. et al. Shortcuts to adiabaticity: Concepts, methods, and applications. *Rev. Mod. Phys.* **91**, 045001 (2019).
33. Schuch, N. & Siewert, J. Natural two-qubit gate for quantum computation using the XY interaction. *Phys. Rev. A* **67**, 032301 (2003).
34. Bialczak, R. C. et al. Quantum process tomography of a universal entangling gate implemented with josephson phase qubits. *Nat. Phys.* **6**, 409–413 (2010).
35. Strauch, F. W. et al. Quantum logic gates for coupled superconducting phase qubits. *Phys. Rev. Lett.* **91**, 167005 (2003).
36. Yamamoto, T. et al. Quantum process tomography of two-qubit controlled-z and controlled-not gates using superconducting phase qubits. *Phys. Rev. B* **82**, 184515 (2010).
37. Ghosh, J. et al. High-fidelity controlled-σ^Z gate for resonator-based superconducting quantum computers. *Phys. Rev. A* **87**, 022309 (2013).
38. Zhang, J., Vala, J., Sastry, S. & Whaley, K. B. Geometric theory of nonlocal two-qubit operations. *Phys. Rev. A* **67**, 042313 (2003).
39. Zhang, J., Vala, J., Sastry, S. & Whaley, K. B. Minimum construction of two-qubit quantum operations. *Phys. Rev. Lett.* **93**, 020502 (2004).
40. Wallraff, A. et al. Approaching unit visibility for control of a superconducting qubit with dispersive readout. *Phys. Rev. Lett.* **95**, 060501 (2005).
41. Yan, F. et al. Tunable coupling scheme for implementing high-fidelity two-qubit gates. *Phys. Rev. Appl* **10**, 054062 (2018).
42. Dogra, S., Vepsäläinen, A. & Paraoanu, G. S. Majorana representation of adiabatic and superadiabatic processes in three-level systems. *Phys. Rev. Res.* **2**, 043079 (2020).

ACKNOWLEDGEMENTS

This work was supported by the Key-Area Research and Development Program of Guangdong Province (Grant No. 2018B030326001), the National Natural Science Foundation of China (Grant No. U1801661, 12004162), Guangdong Provincial Key Laboratory (Grant No. 2019B121203002), the Science, Technology and Innovation Commission of Shenzhen Municipality (Grant No. KYTDPT20181011104202253), Grant No. 2016ZT06D348, the Natural Science Foundation of Guangdong Province (Grant No. 2017B030308003).

AUTHOR CONTRIBUTIONS

Z.T. and L.Z. contributed equally to this work. T.Y. and Z.T. conceived the experiment; Z.T. designed the theoretical protocol and performed the experiment with T.Y. under the supervision of Y.C.; L.Z. designed the superconducting devices used in the experiment, and fabricated them together with Y.Z. and H.J.; T.Y., Z.T., and Y.C. wrote the manuscript together, with inputs from all authors.

COMPETING INTERESTS

The authors declare no competing interests.

ADDITIONAL INFORMATION

Supplementary information The online version contains supplementary material available at https://doi.org/10.1038/s41534-021-00406-1.

Correspondence and requests for materials should be addressed to S.L., T.Y. or Y.C.

Reprints and permission information is available at http://www.nature.com/reprints

Publisher's note Springer Nature remains neutral with regard to jurisdictional claims in published maps and institutional affiliations.